*Astronomy & Astrophysics* manuscript no. XMM-LSS˙II May 5, 2003
(DOI: will be inserted by hand later)

# The XMM-LSS Survey

## II. First high redshift galaxy clusters: relaxed and collapsing systems⋆

Ivan Valtchanov[1], Marguerite Pierre[1], Jon Willis[2], Sergio Dos Santos[1], Laurence Jones[3], Christophe Adami[4], Bruno Altieri[5], Stefano Andreon[6], Micol Bolzonella[7], Pierre-Alain Duc[1], Eric Gosset[8], Christophe Jean[8], and Jean Surdej[8]

[1] CEA/Saclay, Service d'Astrophysique, F-91191, Gif-sur-Yvette, France
[2] ESO, Ave. Alonso de Cordova 3107, Casilla 19, Santiago 19001, Chile
[3] School of Physics and Astronomy, University of Birmingham, Birmingham
[4] LAM, Traverse du Siphon, 13012 Marseille, France
[5] ESA, Villafranca del Castillo, Spain
[6] INAF-Osservatorio Astronomico di Brera, via Brera 28, 20121 Milano, Italy
[7] Istituto di Astrofisica Spaziale e Fisica Cosmica, Sezione di Milano, via Bassini 15, 20133 Milano
[8] Université de Liège, Allée du 6 Août, 17, B5C, 4000 Sart Tilman, Belgium

Received, May 5, 2003, Accepted, May 5, 2003

**Abstract.** We present the first five spectroscopic identifications of new clusters of galaxies at $z > 0.6$ found in the XMM Large-Scale Structure Survey (XMM-LSS). All five candidates are extended X-ray sources in the XMM images. For three of them we have sufficient spectroscopically confirmed member galaxies that an estimate of the velocity dispersion is possible: XLSS-001 at $z = 0.61$ with 29 concordant redshifts, XLSS-002 at $z = 0.77$ with a compact core and 8 galaxies with concordant redshifts at $1.5'$ from the centre and XLSS-003 at $z = 0.84$ with 17 cluster members. The three clusters are at intermediate X-ray luminosities: $L_X \sim 1 - 3 \times 10^{44}$ erg s$^{-1}$ and follow the low redshift scaling relations between $L_X$, $T$ and $\sigma_v$. They have lower temperatures and subsequently are less massive than the previously known clusters at similar redshifts. Thus for the first time we are starting to detect in a systematic way intermediate mass clusters in the high redshift Universe.
Two candidates, XLSS-004 and XLSS-005, cannot be confirmed by these spectroscopic observations, although XLSS-004 is detected independently as an overdensity of galaxies of a colour R-z'=1.4 that matches the redshift of the central galaxy $z = 0.89$. XLSS-005 is a complex system at a redshift around unity associated with an unequivocally extended X-ray source with probable substructure. The X-ray morphology and the distribution of the galaxies with spectroscopic and photometric redshifts in this region point toward an interpretation of two clusters in projection: one at $z \sim 0.95$ and a more distant one at $z \sim 1.02$. Because of their small separation on the sky we are probably detecting for the first time a large-scale structure filament at a redshift of unity as traced by the two clusters.

**Key words.** X-rays: galaxies: clusters; Cosmology: large-scale structure of Universe; Surveys

### 1. Introduction

Statistical samples of distant galaxy clusters can serve as a powerful tool to study the large-scale structure of the Universe. To obtain cluster samples deep enough and over a large area with optical or near-infrared observations is quite a difficult task (e.g. Gunn et al. 1986, Postman et al. 1996, Gonzales et al. 2001, Stanford et al.1997). Projection effects and the small field-of-view of the current NIR imagers interplay to make relatively large contiguous surveys of distant clusters a dubious game.

X-ray observations, by their nature, are much more appropriate and less contaminated by projection effects. From EINSTEIN and ROSAT based X-ray cluster surveys we have gained knowledge about individual objects, scaling relations, the large-scale distribution, the clustering properties and the evolution of galaxy clusters (see Rosati et al. 2002 for a review). With the XMM and Chandra X-ray observatories in orbit we can push the observational limits further. The increased sensitivity can be exploited not only in single deep fields but large areas of the sky can also be surveyed with relatively short exposure times. A

*Send offprint requests to*: Ivan Valtchanov, e-mail: ivaltchanov@cea.fr

⋆ Based on observations obtained with XMM-Newton, CFHT, ESO (program ID: 70.A-0283)

fainter cluster/group population at intermediate redshifts that was not accessible to the previous X-ray missions will thus be detected. In return, this will give us a unique view of the cosmic web as traced by this population.

One of the most important questions is to investigate the clustering properties of the nearby and distant Universe. This is the main scientific goal of the XMM Large-Scale Structure Survey (Pierre et al. 2003, hereafter paperI) – to compute the cluster-cluster correlation function in two redshift bins within $0 < z < 1$. The XMM-LSS survey geometry and depth was chosen such that to have a statistically significant number of objects in these two regions, necessary to improve our knowledge over the results of the ROSAT-ESO Flux Limited X-ray Survey (REFLEX) which covers a much larger area but only reaches $z < 0.2$ (Böhringer et al.1998).

To achieve the objectives of the XMM-LSS we have developed an efficient procedure that uses the full instrument sensitivity and indeed allows us to detect extended sources down to flux levels of $8 \times 10^{-15}$ erg s$^{-1}$ cm$^{-2}$ for 10 ks exposures with XMM (Valtchanov et al. 2001, Dos Santos et al. 2003). The detection is quite crucial because even the mere counting of clusters at different redshifts, the so called cluster abundance evolution, can be used to constrain the cosmological parameters (e.g. Refregier et al. 2002 and references therein) that are complementary and independent to the constraints from the cosmic microwave background and the SN studies.

The first spectroscopic follow-up of the candidate clusters at $z < 1$ was programmed for observations on Las Campanas/Magellan and on the ESO/VLT telescopes. The subject of this paper is to present the first results for a sample of 5 clusters at $z > 0.6$.

The paper is organised as follows: first we present the X-ray data reduction and source detection (Sec. 2), then in Sec. 3 the optical identification, spectroscopic target selection procedure and the observations are described. In Sec. 4 we present the data analysis results from the spectroscopic and X-ray observations. Next we discuss each individual object (Sec.5) and end up with the conclusions (Sec. 6). Except where is mentioned, we use a $\Lambda$CDM cosmology ($H_0 = 70$ km s$^{-1}$ Mpc$^{-1}$, $\Omega_m = 0.3$, $\Omega_\lambda = 0.7$) for all cosmologically dependent parameters.

## 2. X-ray data

The sources for the first spectroscopic run were chosen from all XMM-LSS pointings received by August 2002. This includes 15 AO-1 pointings of 10ks exposures and another 15 of 20 ks exposures from the Guaranteed Time XMM Medium Deep Survey (XMDS, see paperI for details). All observations were of good quality, except two fields that suffered from high background contamination affecting $> 50\%$ of the exposure time.

### 2.1. Data reduction

A detailed description of the pipeline used in the XMM-LSS data reduction will be presented in Dos Santos et al. (2003). Here we just briefly mention the main steps. The X-ray observations were reduced by the standard XMM Science Analysis System (XMM-SAS) tasks `emchain` and `epchain` for MOS and PN detectors respectively. High background periods induced by solar flares were excluded from the event lists and raw photon images in different energy bands were then created. Subsequently the raw images for each instrument were filtered using "à trous" (with holes) iterative wavelet technique with a Poisson noise model and a threshold of $10^{-4}$ (equivalent to $3.7\sigma$ in the Gaussian case) for the significant wavelet coefficients (Starck & Pierre 1998, Starck et al. 1998). Each filtered image is then exposure corrected and a mask map that includes bad pixels, CCD gaps and non-exposed CCD regions (generally parts outside the field-of-view of the telescope) are created. Wavelet-filtered, exposure-corrected images for each instrument in a given energy band are added together to form a total band image to be used in the first stage of the detection procedure.

### 2.2. Source detection

Clusters of galaxies are extended sources in X-ray images and their detection and correct classification is not trivial because of various peculiarities of the X-ray observations: Poisson noise regime, varying PSF as a function of off-axis angle, vignetting effect, and the detector geometry (gaps). We use images in the [0.5-2] keV energy band which is well suited for clusters and groups (Scharf 2002). The detection procedure is based on the prescription of Valtchanov et al. (2001) and has three stages: wavelet filtering (see the previous section), detection and measurements. The wavelet filtered image is fed to `SExtractor` (Bertin & Arnouts 1996) for detection, characterization and classification improved by using weighted images that incorporate the detector masks and bad pixels.

The third step in the detection procedure consists of a maximum-likelihood fit of each source to the PSF, as implemented in the XMM-SAS `emldetect` package, using the `SExtractor` source list as input. The main objective is to improve the source characteristics and classification measurements and obtain the likelihood of the detection and extension (see Dos Santos et al. 2003 for details).

In total, from all available X-ray observations, we find some 55 X-ray cluster candidates from about 3.5 deg$^2$ (30 XMM pointings), which corresponds to $\sim 15$ clusters per sq.deg., in good agreement with the cosmological predictions (see paperI for details).

## 3. Optical data

### 3.1. Optical imaging

Deep images from the CFH12k camera on the Canada-France-Hawaii Telescope (CFHT) in BVRI from the

VIRMOS-VLT Deep Survey (VVDS: Le Fèvre et al. 2001, McCracken et al. 2003) were used for optical identifications. The observations were processed by the Terapix team[1] to produce astrometrically and photometrically calibrated images and to create object catalogs by means of `SExtractor`. The definition and magnitude limits of the VVDS may be found in the web pages of the VIRMOS consortium[2]. The X-ray cluster candidates were assigned to *NEAR* ($z < 0.5$) and *MID* ($0.5 < z < 1$) samples by visual inspection of the optical images and also using photometric redshift estimates (paperI). The visual scan of the data was also indispensable for removal of spurious extended sources introduced by instrumental effects or by the iterative wavelet filtering procedure. In addition to the CFH12k data, we obtained observations at the CTIO 4m telescope in R and z' which allowed us to search for a red sequence of galaxies at a given X-ray position (Andreon et al. 2003a).

### 3.2. Spectroscopic target selection

Our driving objective was to confirm the clusters and to measure their redshifts. We chose the ESO-VLT/FORS2 instrument in MXU multi-objects spectroscopy mode because of the liberty to place a large number of slits with different sizes and orientations and so to optimize the target selection, especially in regions of high galaxy density. Using `fims` (the FORS Instrumental Mask Simulator tool), we placed about 30 slits on average in each mask, eventually placing inclined and longer ones. We also randomly sampled the X-ray QSO population presented in the same area with the remaining available slits.

We have developed a visualization procedure to facilitate the selection of spectroscopic targets, optimizing the chances to pick up cluster member galaxies. It uses all the available information in the field, combining optical (one band or pseudo-colour VRI image) and X-ray images, colour-magnitude and colour-colour diagrams, and photometric redshift peaks and probabilities (see paperI for details). In this "multi-parametric space", first we have taken the objects above the photometric limit, imposed by exposure time and observational strategy constraints. Secondly, we have looked for objects with a plausible colour (V-I or R-I) for ellipticals at the estimated photometric redshift and also used the pseudo-colour images for all candidates for which we have had V, R and I observations. The utility of colour information is justified as out to redshift of unity the major population of cluster cores is made of ellipticals with an old stellar population (e.g. Dressler et al. 1997, Postman et al. 1998). Moreover, cluster ellipticals at high redshift show-up as an overdensity of red objects in VRI composite images, proving useful in the target selection process. Examples of RGB images for some of the candidate clusters can be found in the web pages of the XMM-LSS consortium[3]

### 3.3. Spectroscopic observations

The ESO-VLT/FORS2 spectroscopic observations in MXU mode were performed on 9-12 October 2002. For the allocated 3 nights in "visitor" mode we selected some 12 candidates from the *NEAR* and *MID* samples. *NEAR* clusters were included in order to provide targets in case of a poor weather and will be presented elsewhere (Willis et al. 2003). The observing log and object designations for the 5 clusters pertaining to this paper, that fall in the *MID* sample and at $z > 0.6$, are shown in Table 1.

We have used the holographic grism 600RI+19 with the GG435 blocking filter that gives a good response from about 5000 to 8500 Å and a dispersion of 1.64 Å/pixel with the standard instrument resolution. The spectral resolution for slits of $1.4''$ width as measured from the arc or sky lines was $\sim 6$ Å FWHM. The high resolution of the grism ($\lambda/\Delta\lambda = 1000$) makes subsequent sky subtraction easier.

For each mask we split the total observing time into two exposures in order to remove the cosmic ray contaminations with `IRAF/imcombine` task and `crreject` algorithm that is appropriate for rejecting cosmic ray events even with two images. The spectral reduction was performed using the standard tools from `IRAF`: zero level exposure, flat-fielding, cosmic ray removal, aperture selection and sky subtraction using the `apextract` package. For wavelength calibration we have used He-Ne-Ar lamp exposures observed at the end of the corresponding night. The wavelength calibration was performed with a Chebyshev polynomial of 3rd degree and the residuals were kept inside $\pm 1.0$ Å with an rms $\sim 0.3-0.5$ Å. A standard star was observed in the beginning and at the end of each night with the same instrumental configuration in order to remove the instrumental response and therefore to transform the spectra to relative flux units.

As an example, in Fig. 1 we show the spectra of the brightest cluster galaxies (BCG).

## 4. Results

### 4.1. Redshifts

The sky subtracted, wavelength and flux calibrated spectra were used to derive the redshifts. First we obtained a redshift estimate based on the CaII H+K doublet, when present, and then we used the cross-correlation technique as implemented in the `RVSAO` package (Kurtz & Mink 1998) using an elliptical galaxy template spectrum (Kinney et al. 1996). To improve the cross-correlation signal we have masked the wavelength ranges of the strongest sky lines, where residuals from the sky subtraction could occur, and also the region of a strong atmospheric absorption at 7750-7800 Å.

[1] http://terapix.iap.fr

[2] http://www.astrsp-mrs.fr/virmos/vvds.htm

[3] http://vela.astro.ulg.ac.be/themes/spatial/xmm/LSS

**Table 1.** ESO-VLT observing log. The exposure time is given for each mask.

| ID[a] | Cluster | R.A. (J2000.0) | Decl. | Seeing arcsec | Exposure min. |
|---|---|---|---|---|---|
| | | 09-Oct-2002 | | | |
| 001 | XLSSJ022457.1−034853 | 02:24:57.1 | −03:48:53 | 1.0-1.2 | 2x60 |
| 005 | XLSSJ022709.7−041805 | 02:27:09.7 | −04:18:05 | 0.7-1.1 | 2x90 |
| | | 10-Oct-2002 | | | |
| 004 | XLSSJ022530.2−050713 | 02:25:30.2 | −05:07:13 | 0.8-2.7 | 90+60 |
| | | 10-Oct-2002 | | | |
| 002 | XLSSJ022532.5−035510 | 02:25:32.5 | −03:55:10 | 0.7-1.2 | 2x60 |
| 003 | XLSSJ022737.6−031807 | 02:27:37.6 | −03:18:07 | 0.7-1.1 | 2x60 |

[a] - In the following, all clusters are referred to via the reference XLSS-plus the identification number, e.g. XLSS-001, etc.

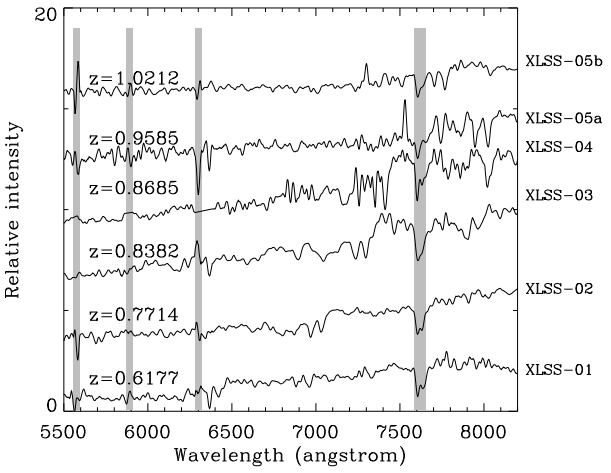


**Fig. 1.** Spectra, with the corresponding redshift, of the brightest or centrally located cluster galaxies with respect to the observed wavelength. The regions with residuals from the sky subtraction are masked with grey bands and the spectra are smoothed with a boxcar of $\sim 11$Å.

The redshift distributions in each field are shown in Fig. 2. To illustrate the redshift space overdensities we have applied an adaptive kernel smoothing over the redshifts – the so called adaptive kernel density estimation (e.g. Silverman 1986, Pisani 1993). There is both a clear redshift grouping and a spatial grouping associated with the X-ray emission in XLSS-001, XLSS-002 and XLSS-003. For these three cases only we show zoomed in an inset a redshift histogram of the overdensity with a fixed bin size. The derived mean redshift and the velocity dispersion, by means of the bi-weighted estimators of location and scale (Beers et al. 1990), are shown in Table 2; the quoted errors are $1\sigma$ bias-accelerated bootstrap errors (Efron & Tibshirani 1986).

For XLSS-004 and XLSS-005 the peaks in the redshift distribution do not correspond to any significant spatial clustering, and no peak can be unambiguously associated with an X-ray source. Nevertheless, we show in Table 2 the most plausible redshift based on measurements of galaxies most likely associated with the cluster X-ray emission (see Figs. 8 and 9).

**Table 2.** Cluster redshift characteristics. $N_{gal}$ shows the total number of galaxies used to derive the redshift. The number in parenthesis shows the number of emission line galaxies.

| Name | Redshift | $\sigma_v$ km/s | $N_{gal}$ |
|---|---|---|---|
| XLSS-001 | $0.6136^{+0.0007}_{-0.0006}$ | $947^{+160}_{-91}$ | 29(9) |
| XLSS-002* | $0.7720^{+0.0006}_{-0.0007}$ | $560^{+410}_{-130}$ | 8(5) |
| XLSS-003 | $0.8378^{+0.0007}_{-0.0006}$ | $780^{+120}_{-75}$ | 17(5) |
| XLSS-004 | $\sim 0.88$ | — | 2 |
| XLSS-005 | $\sim 1.0$ | — | 7(5) |

(*) – taking only the objects inside the core (at less than $1'$ from the centre) and $0.76 \leq z \leq 0.78$.

### 4.2. X-ray analysis

For each cluster an X-ray spectrum was extracted from a region large enough to include the cluster emission. A background spectrum was taken from an adjacent annulus. We removed in advance the contribution of all other sources within the cluster and background regions. A photon redistribution matrix (RMF) and ancillary region file (ARF) were created using `XMMSAS:rmfgen/arfgen`, including corrections for bad pixels and detector geometry. Finally the spectra from the three instruments MOS1, MOS2 and PN were regrouped to have at least 25 counts per bin. The extracted spectra were used to derive the observed characteristics shown in Table 3 without any recourse to a reference model.

To derive the global cluster X-ray characteristics, the binned spectra in each instrument were fitted to a `mekal` model of thermal plasma emission with photo-electric absorption using `XSPEC` (Arnaud 1996, also see the `XSPEC` manual[4] for the `mekal` model and corresponding references). We have kept only two free parameters, which are the temperature and the normalisation. The mean Galactic absorption of $N_H = 2.5 \times 10^{20}$ cm$^{-2}$ (Dickey & Lockman 1990), the metal abundance of $Z = 0.3 Z_{\odot}$ and

[4] http://heasarc.gsfc.nasa.gov/docs/xanadu/xspec/manual/

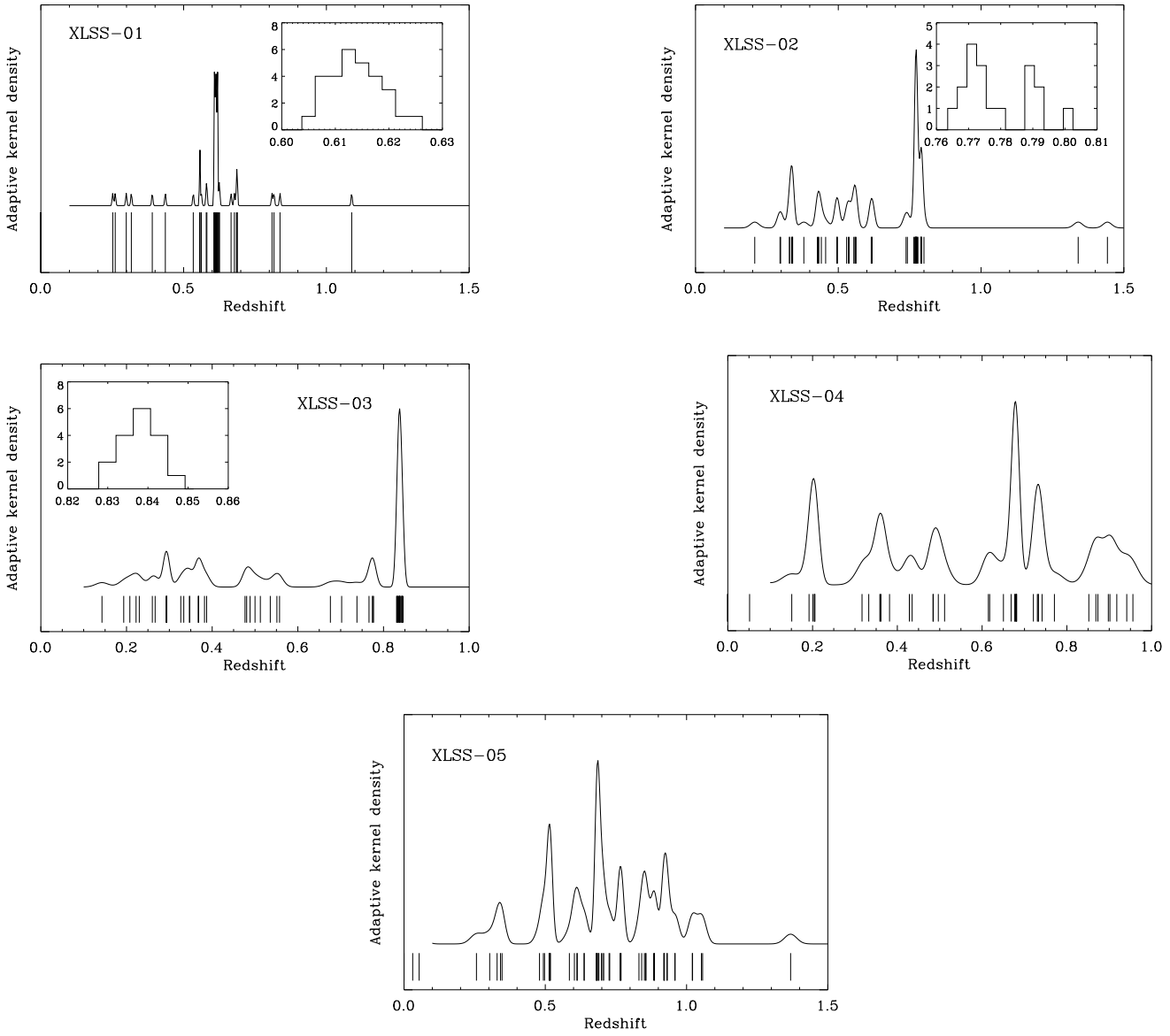


**Fig. 2.** Redshift distributions of the spectroscopically observed objects for all five clusters. The adaptive kernel density estimation (Silverman 1986) is shown as a continuous line over the redshift measurements. In cases where an overdensity in redshift space corresponds to a spatial correlation we show a histogram of the zoomed redshift region: for XLSS-001 from 0.6 to 0.63, bin size 0.0025; XLSS-002: $0.76 < z < 0.82$, bin size 0.003; XLSS-003: $0.82 < z < 0.86$, bin size 0.0043.

the redshift were fixed. For parameter estimation we used the Cash statistic, modified to allow background subtraction (see the `XSPEC` manual). The results for XLSS-001, XLSS-002 and XLSS-003 are shown in Table 4. For the other two candidates the photon statistics are insufficient to allow any plausible parameter estimation. The X-ray spectra, `mekal` fit and the corresponding $\chi^2$ residuals are shown in Fig. 3.

The bolometric X-ray luminosity $L_X$ was calculated using the full energy range, constrained only by the instrument response matrices (generally from $\sim 0.05$ to $\sim 20$ keV rest frame). The cluster masses were estimated from the local $L_X - M$ relation (Reiprich & Böhringer 2002) assuming no evolution.

### *4.3. Scaling relations*

The scalings between the bolometric luminosity, temperature and velocity dispersion from the clusters in the compilation of of Wu et al. (1999) are shown in Fig. 4, together with the objects presented in this paper. XLSS-001, XLSS-002 and XLSS-003 are in good agreement with the scaling relations $L_X - \sigma_v$ and $L_X - T$ (Xue & Wu 2000, Arnaud & Evrard 1999), although caution must be taken because of possible biases on the temperature introduced by the insufficient photon statistics (see e.g. Fairley et al. 2000). What is important to note is that the three clusters are at lower temperatures and luminosities than the other known clusters at high redshift. In that sense we are start-

**Table 3.** X-ray parameters of the *MID* sample. "Region" is the extraction radius in arcmin and in comoving Mpc in brackets. "$R_{50}$" is the object's half-light radius in arcsec in the [0.5-2] keV band. The "Exposure" is the average of the weighted live time events in the extraction region.

| Name | Redshift | Region | $R_{50}$ | Counts [0.2-10] keV | Exposure MOS1+MOS2+PN |
|---|---|---|---|---|---|
| | | arcmin(Mpc) | arcsec | ALL(MOS1+MOS2+PN) | ks |
| XLSS-001 | 0.6136 | 1.7(0.78) | 32.2 | 1693(431+438+824) | 2x13.3+7.9 |
| XLSS-002 | 0.7720 | 1.1(0.60) | 16.6 | 481(126+101+254) | 2x13.3+7.9 |
| XLSS-003 | 0.8378 | 1.1(0.65) | 23.6 | 458(101+78+279) | 2x11.5+8.3 |
| XLSS-004 | $\sim 0.88$ | 0.5(0.27) | — | 233(40+83+110) | 2x20.8+16.6 |
| XLSS-005 | $\sim 1.0$ | 0.83(0.56) | 21.1 | 353(50+76+227) | 24.5+24.9+21.5 |

**Table 4.** Derived, model dependent, cluster X-ray characteristics. No data is presented for XLSS-004 and XLSS-005 because of the poor photon statistics.

| Name | Redshift | $kT$ | $F_X^a$ keV | $L_X^b$ | $M^c$ |
|---|---|---|---|---|---|
| XLSS-001 | 0.6136 | $3.1^{+1.0}_{-0.6}$ | 8.2 | 2.8 | 6.8 |
| XLSS-002 | 0.7720 | $2.2^{+1.3}_{-0.6}$ | 2.6 | 1.2 | 4.1 |
| XLSS-003 | 0.8378 | $4.2^{+5.3}_{-1.9}$ | 4.4 | 3.1 | 7.1 |

[a] – the unabsorbed flux $F_X$ in the [0.5-2] keV band and in units of $10^{-14}$ erg s$^{-1}$ cm$^{-2}$.
[b] – the luminosity $L_X$ is bolometric and in units of $10^{44}$ erg s$^{-1}$.
[c] – the mass $M$ in units of $10^{14}\,M_\odot$.

ing to reach moderately massive systems at high redshift, whilst from ROSAT or EINSTEIN deep surveys the distant clusters are rather more luminous and consequently more massive systems.

## 5. Individual objects

The optical/X-ray overlays for all candidates are shown in Figs.5-9. The optical images are from CFH12k in the I-band, and the X-ray contours are from wavelet filtered, summed MOS1&2+PN images (see Sec. 2). For XLSS-001, XLSS-002 and XLSS-003 the objects from the inset histograms of their redshift distribution (Fig. 2) are denoted as boxes and triangles, the latter for the galaxies with emission lines. When there was no obvious redshift peak (XLSS-004 and XLSS-005) we indicate in the figure the redshift measurements of each spectroscopically observed galaxy.

Based on the morphology, redshift distribution and the visual appearance we define three broad cluster classes: relaxed, relaxing and collapsing.

### 5.1. Relaxed cluster: XLSS-003

This has the appearance of a relaxed, distant cluster at $z = 0.8378$ with a velocity distribution close to a Gaussian. Normality tests (Anderson-Darling and Shapiro-Wilk, see e.g. D'Agostino & Stephens 1986) accept the null hypothesis of the distribution being drawn from a normal distribution at 90% confidence, but this must be taken with caution as the number of objects is small. The X-ray emission is slightly elongated and there is no evidence of substructure. The brightest cluster galaxy coincides with the X-ray emission peak and is at rest with respect to the cluster mean ($z_{BCG} = 0.8382$, $\Delta v = 65$ km s$^{-1}$).

As can be seen from Tabs. 3 and 4, the low photon statistics do not allow the temperature to be constrained, although if we assume an equipartition between the galaxy velocities and the gas, i.e. $kT = \mu m_p \sigma_v^2$, we derive a temperature of $kT = 3.9 \pm 1.5$ keV – in excellent agreement with the best fit value.

### 5.2. Relaxing cluster: XLSS-001

Morphologically XLSS-001 at $z = 0.6136$ looks like present day still relaxing clusters: there is an obvious centre formed by the brightest cluster galaxies displaced at $\sim 30''$ from the X-ray emission peak, there is a subclump to the north-east and the brightest cluster galaxy (BCG) that has a typical giant elliptical galaxy absorption spectrum (see Fig. 1) is at 750 km s$^{-1}$ from the mean cluster redshift. The velocity distribution is quite broad, but the normality tests accept at the 90% confidence level the null hypothesis that the observed distribution is consistent with a normal distribution.

There are three other X-ray sources projected over the cluster emission. One is the subclump to the north-east, which is most likely associated with a group falling into the cluster potential as there are three cluster members within the X-ray contours (two of which are emission line galaxies) and no obvious optical counterpart at the X-ray peak. Another X-ray source is visible to the north and is probably associated with a nearby galaxy. Finally to the south-east there is a bright point-like source for which we do not have the optical spectrum.

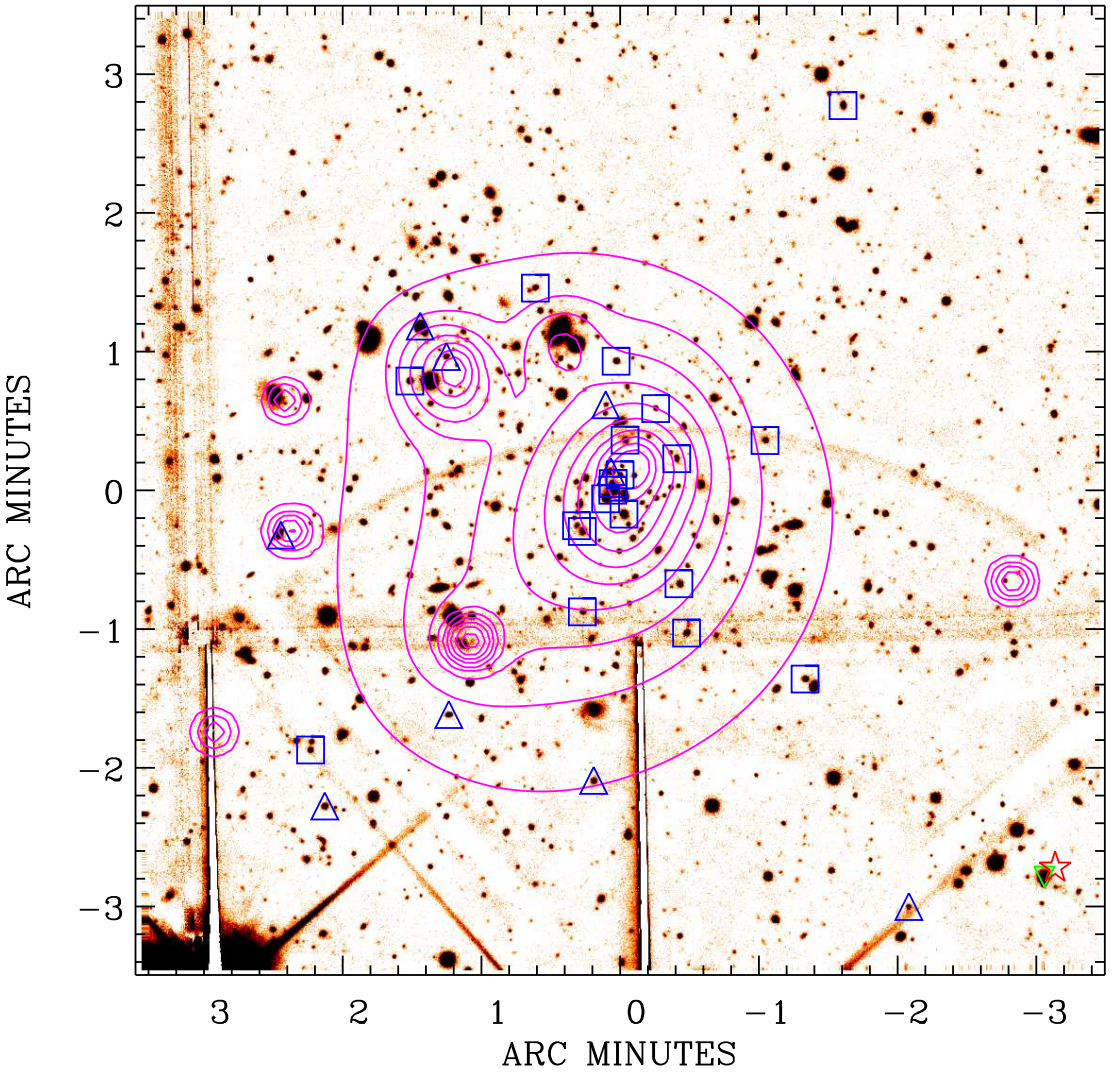


**Fig. 5.** XLSS-001. CFH12k I-band image of a $7' \times 7'$ field is shown. North is up and east to the left. The X-ray contours run from 0.5 to 5 counts/pixel with 10 levels in log space. Objects in the $0.6 \leq z \leq 0.63$ redshift range are denoted by boxes and triangles (for emission-line objects). [*See the electronic edition of the journal for a colour version of this figure*]

The X-ray characteristics of the cluster are well constrained as we have about 1600 photons in the spectrum and the cluster is of low temperature. The low luminosity of the cluster is in agreement with its temperature but is at variance with the velocity dispersion (see e.g. Fig. 4). This may be regarded as an another argument for the cluster being in the process of relaxation. The gas may have already settled down in the potential whilst the galaxies have still to relax.

### *5.3. Collapsing cluster: XLSS-002*

Although XLSS-002 resembles a point-like source in X-rays, its half-light radius is $R_{50} \approx 17''$ (see Table 3, to be compared to the PSF half-energy width of $16''$) but the extension likelihood (from `emldetect`) is 7.4, corresponding to a probability of $6 \times 10^{-4}$ of being a point-like source. The 8 centrally located galaxies form a crown-like figure, and five are in very narrow redshift range $0.771 - 0.775$ most likely forming a compact core. There are galaxies at similar redshifts all over the field as can be seen in Fig. 6. None of the other X-ray sources present in the field are cluster members.

The temperature is quite tightly constrained by the X-ray spectral fit as the cluster has a rather low temperature even though the photon statistics are poor – 480 photons in the [0.2-10] keV band in total. There is a large fraction of emission-line galaxies in the centre (5 from 8) and probably some of them, if shown to be AGNs, might contribute to the overall X-ray emission.

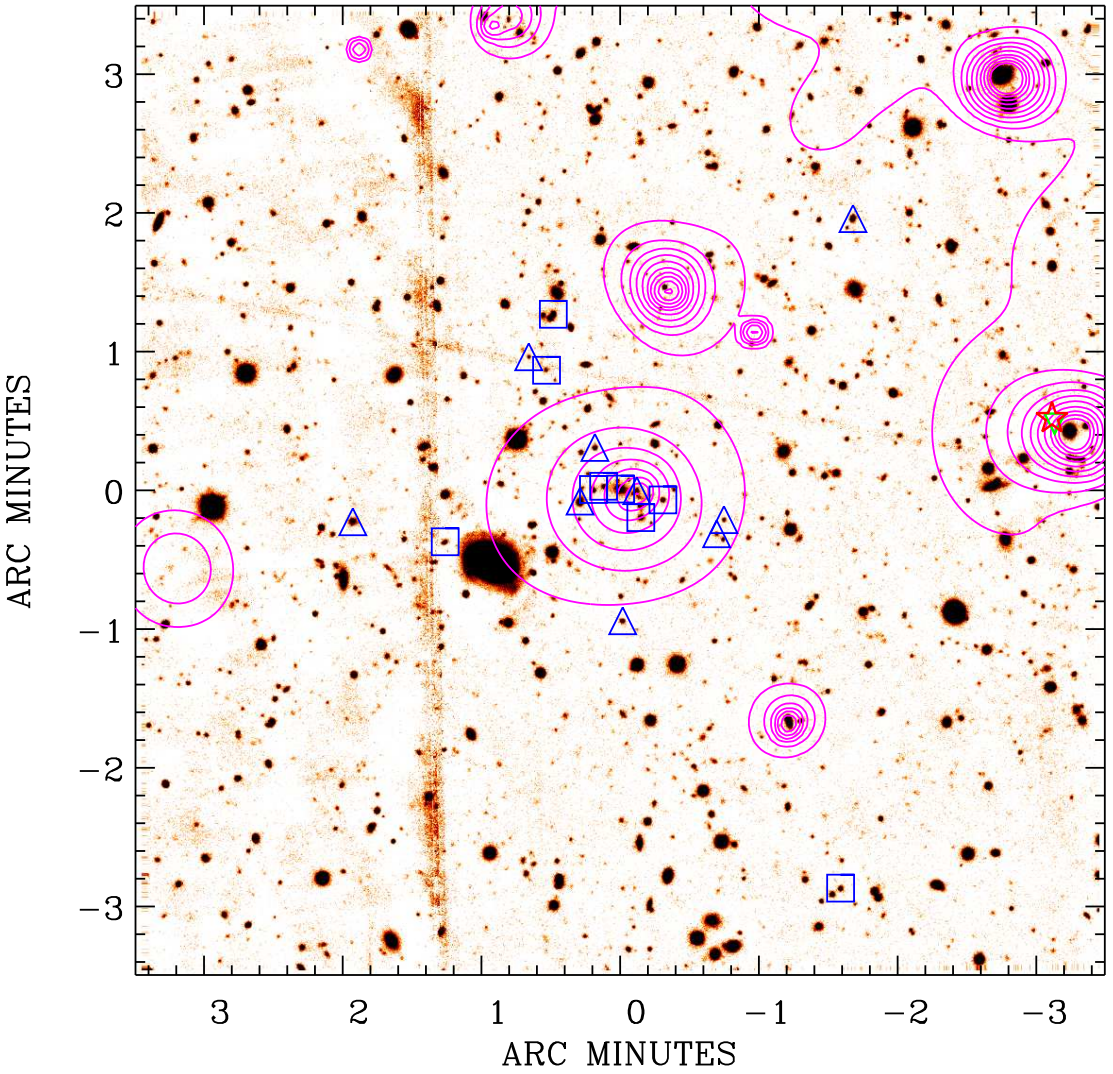


**Fig. 6.** XLSS-002. A $7' \times 7'$ field is shown and the objects at $0.76 \leq z \leq 0.82$ are denoted by boxes and triangles (for emission-line objects). The X-ray contours run from 0.1 to 5 photons/pixel with 10 levels in log space, with the lowest cluster contour at 0.1 photons/pixel. [*See the electronic edition of the journal for a colour version of this figure*]

The brightest cluster galaxy, at a redshift coinciding with the mean of the centrally located galaxies ($z_{BCG} = 0.7714$, Fig. 1) has a typical giant elliptical galaxy absorption spectrum.

Based on the morphology and the redshift distribution, the most plausible interpretation is that the cluster is in its early stage of formation: a compact core is already formed and the accretion of matter from the nearby large-scale structure is underway. The agreement between the cluster global characteristics, $L_X$, $T$ and $\sigma_V$ (Fig. 4) is quite striking, but shows that no violent shocks or other non-gravitational processes are occurring at this stage.

### 5.4. Other cases

*XLSS-004* The cluster X-ray emission lies between two bright X-ray sources identified as QSOs at $z = 1.12$ (the closest to the north-west, with 486 counts in the [0.5-5] keV band and V = 21.2, R = 20.9, I = 20.8) and at $z = 1.19$ (to the south-east, with 378 counts and V = 18.5, R = 18.5, I = 18.0). These two QSOs are located in diametrically opposed directions at 0.9' and 1.2' from the centre of the cluster X-ray emission, respectively. Such a configuration is very unlikely to occur by chance. Given our estimated surface density of approximately 30 X-ray sources per deg$^2$ over a field of 2.8 deg$^2$ in the XMM-LSS survey with detected counts greater than 300, the probability of detecting two X-ray sources within 2' from

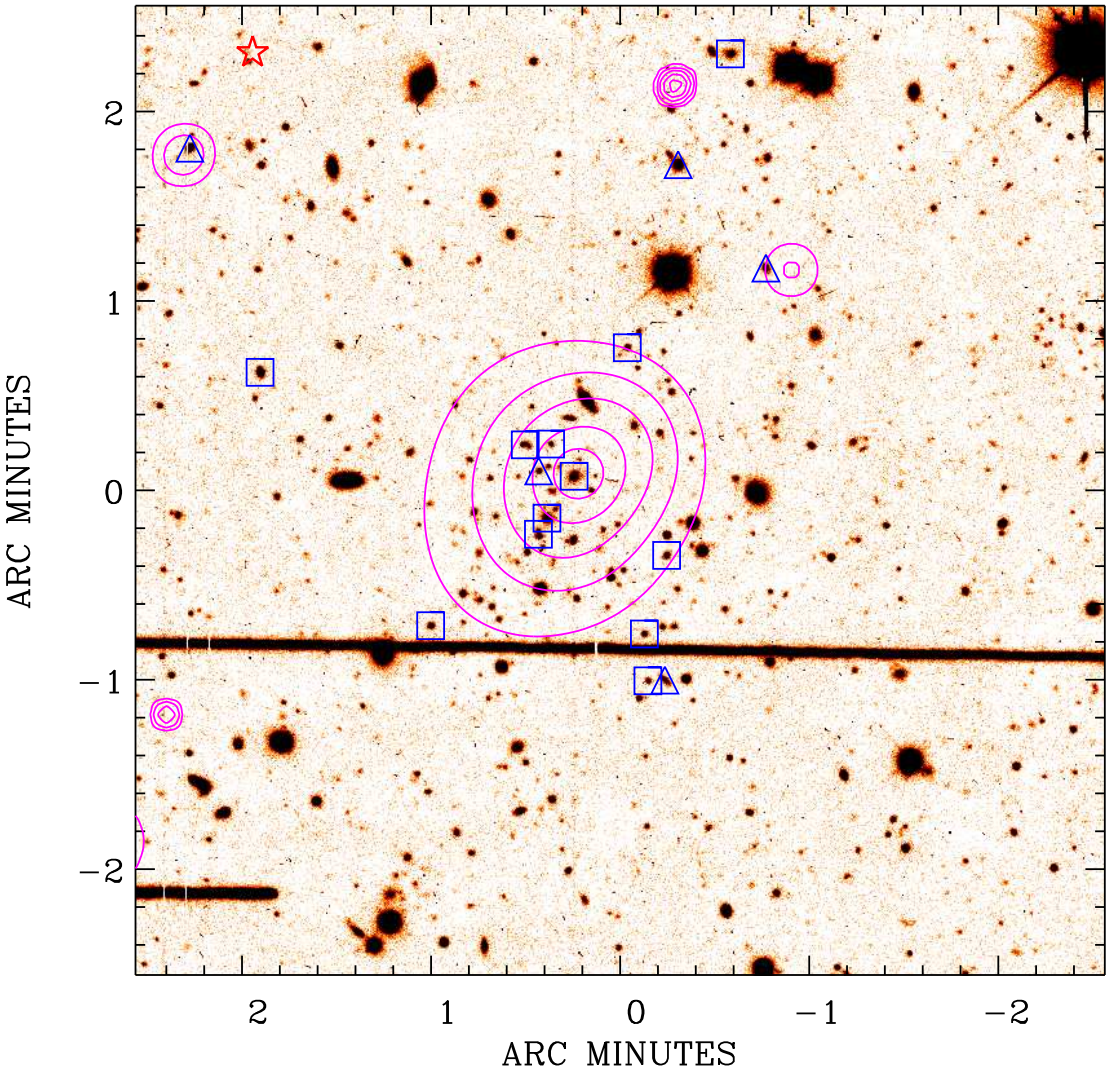


**Fig. 7.** XLSS-003. Only the central $5' \times 5'$ region of the field is shown and the objects in $0.82 \leq z \leq 0.86$ are denoted by boxes and triangles (for emission-line objects). The X-ray contours run from 0.1 to 5 photons/pixel with 10 levels in log space, and the lowest cluster contour is at 0.1 photons/pixel.[*See the electronic edition of the journal for a colour version of this figure*]

the cluster X-ray centre is about 1%. Given that these two quasars are located just behind a putative foreground cluster at z = 0.9 (see below), gravitational lensing could possibly affect the real positions and fluxes of these two background objects. However, the hypothesis that these QSOs could be two images of a single source lensed by a foreground cluster does not hold as their optical spectra show a significant redshift difference $\Delta z \simeq 0.07$. A more detailed discussion on this unusual association will be presented elsewhere (Jean et al. 2003).

We cannot confirm the reality of the cluster from the spectroscopic observations only – the galaxy coincident with the peak of the X-ray emission is at $z = 0.868$ and there is only one other galaxy $30''$ to the south-east at a similar redshift, $z = 0.873$. XLSS-004 is, however, independently detected on a scale of 1 arcmin diameter (marked as a thick green circle in Fig. 8) as an overdensity of galaxies with a similar colour of R-z'= $1.4^m$, corresponding to $z \approx 0.9$ (Andreon et al. 2003a). The cluster optical luminosity function also suggests a high redshift, compatible with $z = 0.9$ (Andreon et al. 2003b).

There is a peak in the redshift distribution at $z \approx 0.68$ (see Fig. 2) but it does not correspond to any spatial grouping.

*XLSS-005* This is a very interesting and complicated case with probably two structures in projection, at $z \sim 0.95$ and $z \sim 1.02$. The morphology of the X-ray emission also suggests a bi-modality, with a central extended source and a possible subclump to the south-east. It is not trivial, however, to disentangle the centre, where galaxies

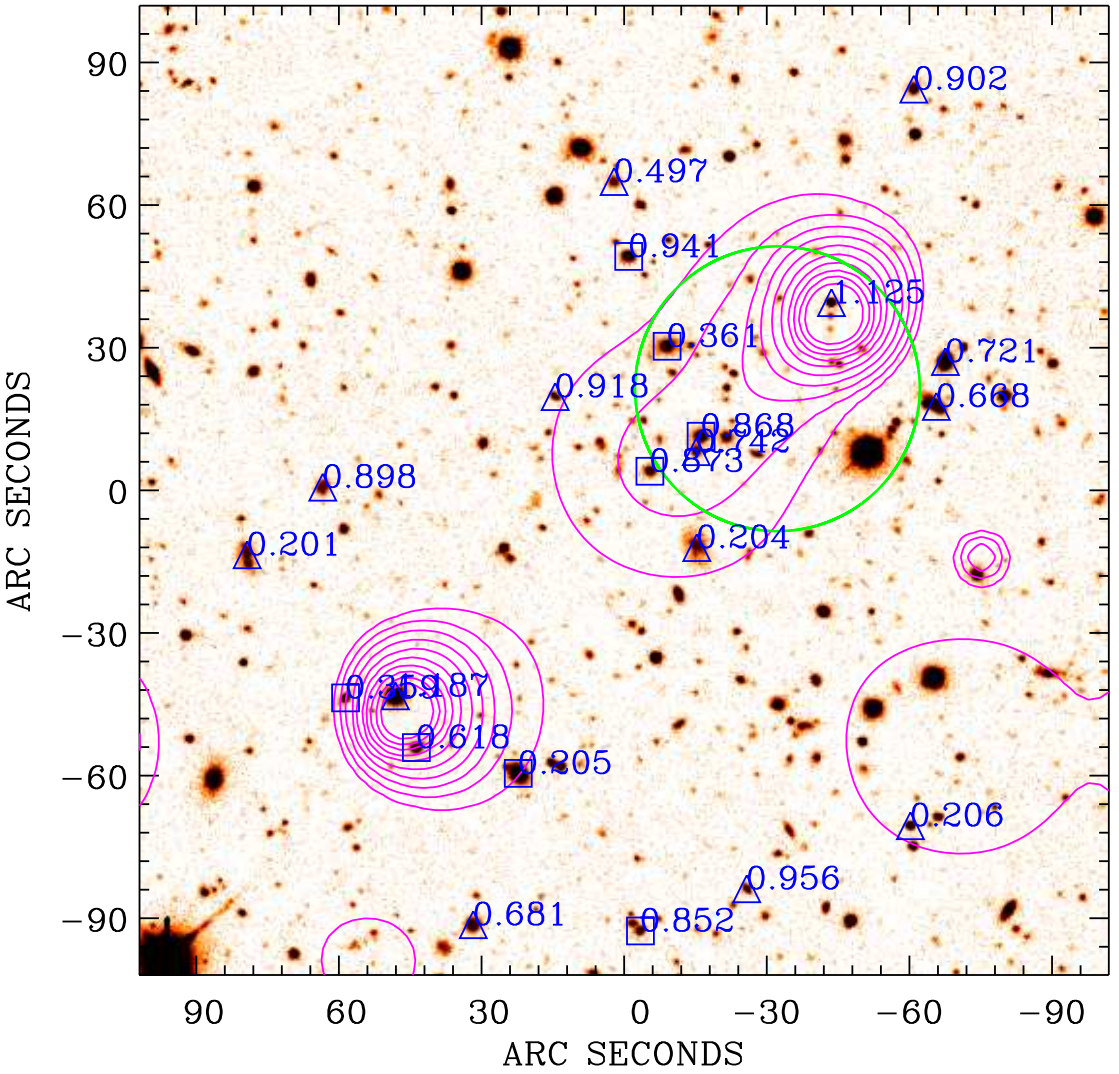


**Fig. 8.** XLSS-004. Only the central $3' \times 3'$ region of the field is shown and the redshifts for all spectroscopically observed objects are indicated. The triangles denote emission-line objects. The X-ray contours run from 0.15 to 5 photons/pixel with 10 levels in log space, with the lowest cluster contour at 0.15 photons/pixel. The optical detection from CTIO Rz' data is shown as a green circle.[*See the electronic edition of the journal for a colour version of this figure*]

at $z = 0.92 - 0.96$ and $z = 1.02 - 1.06$ are mixed. The redshift space distance between the two groups is rather significant: $\Delta z \sim 0.1$ ($\sim 15000$ km s$^{-1}$) which rules out the galaxies belonging to the same cluster.

This cluster has already been observed in the K' band with ESO-NTT/SOFI in the framework of the XMM-LSS VIRMOS Deep Survey over an area of 0.25 deg$^2$. The exposure of 1.5 hours resulted in a catalog down to a limiting magnitude K'$_{AB} \approx 22.7$. A search for overdensities in photometric redshift slices of $\Delta z_{phot} = 0.2$ was made, with $z_{phot}$ calculated from BVRIK' photometry. As a result, there is a strong detection with signal-to-noise (S/N) $\sim 5$ of an overdensity at $z \approx 0.9$ centred on the south-east extension of the X-ray emission. Observations in J and K at ESO-NTT/SOFI (Andreon et al. 2003b) also indicate two overdensities of galaxies with colours compatible with $z \approx 1$.

Our preliminary interpretation is that we are observing two clusters in projection: one at $z \sim 0.92 - 0.95$, forming the main body of the extended X-ray source, and the more distant one at $z = 1.02 - 1.05$, that is partially covered. The redshifts of the spectroscopically observed objects, that span all of the interval from $z \sim 0.92$ to $z \sim 1.05$, could be an indication of a filament connecting both clusters. However, their number is insufficient for any strong claim. This is a good target for deep integral field spectroscopy observations (e.g. IFU of the VIMOS instru-

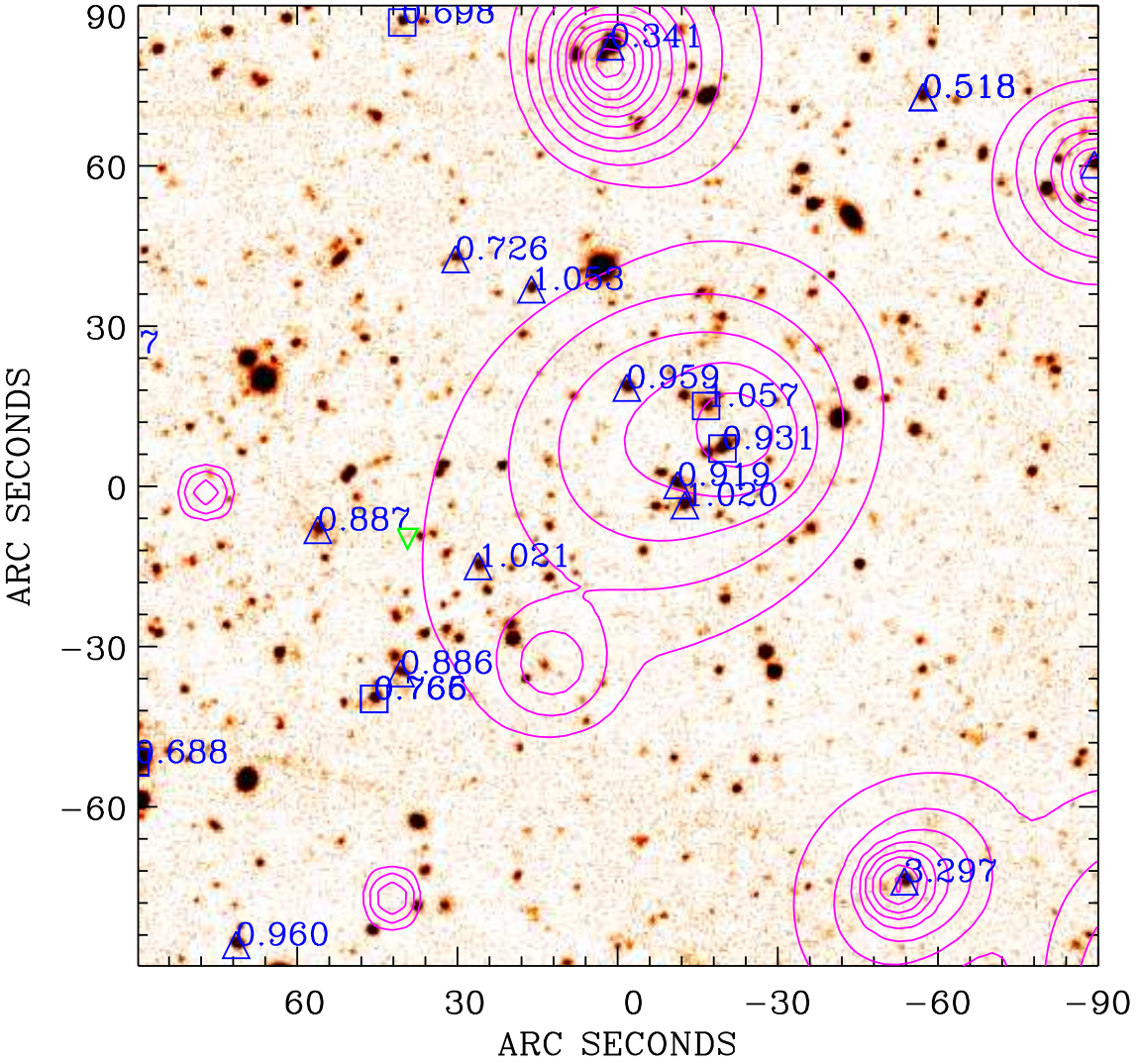


**Fig. 9.** XLSS-005. Only the central $3' \times 3'$ region of the field is shown and the redshifts for all spectroscopically observed objects are indicated. The triangles denote emission-line objects. The X-ray contours run from 0.15 to 5 photons/pixel with 10 levels in log space, with the lowest cluster contour at 0.15 photons/pixel.[*See the electronic edition of the journal for a colour version of this figure*]

ment) that will help us resolve this extremely interesting case.

The large fraction of emission line objects is also striking. Of 7 objects in the centre with redshifts between $0.92-1.06$, 5 have detectable [OII]3727Å emission in their spectra.

## 6. Conclusions

We present spectroscopic confirmation of the first high redshift, X-ray selected clusters in the XMM Large-Scale Structure Survey. The detection and classification in X-rays, the subsequent optical identification and spectroscopic target selection demonstrate the efficiency of the follow-up procedure.

### 6.1. Highlights

- Five newly discovered X-ray clusters from the *MID* sample at $z > 0.6$ were observed at ESO-VLT for 11.5 hours in total. For three of them we measured more than 15 galaxies with concordant redshifts and thus obtained a viable estimate of the velocity dispersion.
- Thanks to the optimized target selection we were able to get an estimate of the velocity dispersion of XLSS-003 at $z = 0.84$ in a reasonable VLT time of 2 hours. To show the potential of the XMM-LSS it is interesting

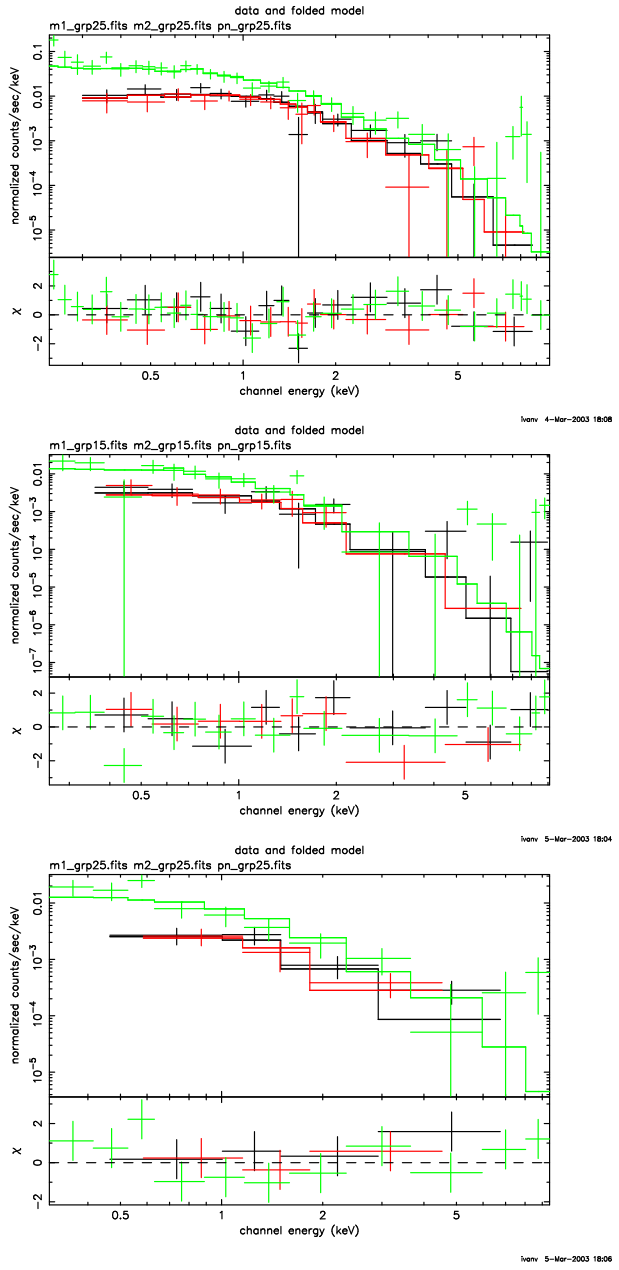


**Fig. 3.** X-ray spectra, model fit (continuous histogram) and the corresponding distribution of $\chi^2$ for MOS1 (black), MOS2 (red) and PN(green). From top to bottom the objects are XLSS-001, XLSS-002 and XLSS-003. The spectra were initially regrouped to have at least 25 photons per energy bin.[*See the electronic edition of the journal for a colour version of this figure*]

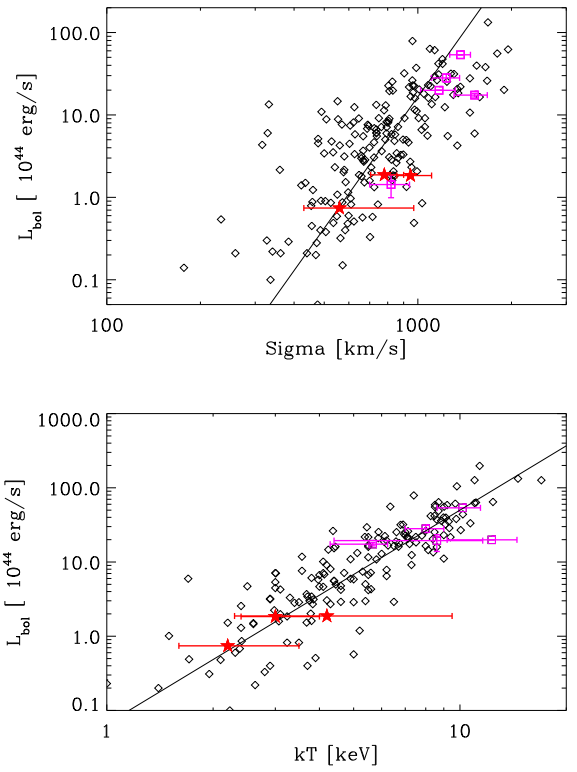


**Fig. 4.** The scaling relations: luminosity-velocity dispersion ($L_X - \sigma_v$, upper panel) and luminosity-temperature ($L_X - T$, lower panel). The clusters from the compilation of Wu et al. (1999) are denoted as diamonds and those at $z \geq 0.5$ are shown as magenta boxes with error bars. The best fit from Xue & Wu (2000) for $L_X - \sigma_v$ and from Arnaud & Evrard (1999) for $L_X - T$ are shown as lines. The objects pertaining to this paper are shown as filled red stars with the corresponding error bars. [*See the electronic edition of the journal for a colour version of this figure*]

to note that to date (March 2003) there are 5 known clusters in the literature (two of them are X-ray selected) at $z > 0.8$ with more than 10 spectroscopically measured concordant redshifts, allowing an estimate of the velocity dispersion.

– We have detected a complex structure at a redshift of unity – XLSS-005. Most likely there are two clusters at $z \sim 0.9$ and $z \sim 1$ observed in projection, the signature of which is also detected in X-rays. Galaxy overdensities in the same region in photometric redshift slices around $z \sim 0.9 - 1$, together with the large span of spectroscopic redshifts of the objects in the central region, are indications that we are seeing a large-scale filament in projection.

– One cluster, XLSS-004, is not confirmed by the spectroscopic run alone, but the CTIO Rz' observations detect it as an overdensity of R-z'=$1.4^m$ galaxies, matching the redshift, $z \sim 0.9$, of the centrally located galaxy.

– From Tables 3 and 4, and Fig. 4, it is obvious that for the first time we are unveiling moderate mass clusters in the redshift range $0.5 < z < 1$. Most of these objects are weak, moderately extended X-ray sources and consequently would have been missed or incorrectly classified in deep ROSAT pointings because of the insufficient photon statistics in addition to the worse PSF. Thus with XMM-LSS we are starting to fill the cluster database with objects at high redshift from the middle of the mass function. This is very important, first for cosmological constraints and second, for non-gravitational physics in clusters (as the effects like pre-

heating and feedback are presumably more important in lower mass systems).

### 6.2. Prospects

In the near future, our goal will be to confirm via spectroscopic identifications all XMM-LSS clusters down to $\sim 8 \times 10^{-15}$ erg s$^{-1}$ cm$^{-2}$ over the 3 sq.deg. of the AO-1 observations. This will form a complete sample of about 30 X-ray selected clusters at $0 < z < 1$. A follow-up of the most interesting objects at $z \sim 1$ is also previewed with integral-field spectroscopy.

*Acknowledgements.* SDS is supported by a post-doctoral position from the Centre National d'Etudes Spatiales. MP and IV are grateful to the ESO/Santiago Office for Science, for a 2 week stay in October 2002, were the the analysis of the VLT data presented here was initiated.

This research has made use of the X-Rays Clusters Database (BAX) which is operated by the Laboratoire d'Astrophysique de Midi-Pyrénés (LAOMP), under contract with the Centre National d'Etudes Spatiales (CNES); the NASA/IPAC Extragalactic Database (NED) which is operated by the Jet Propulsion Laboratory, California Institute of Technology, under contract with the National Aeronautics and Space Administration.

## References

Andreon S. et al., 2003a, in preparation
Andreon S. et al., 2003b, in preparation
Arnaud K.A., 1996, in ASP Conf. Ser., Vol. 101, Astronomical Data Analysis Software and Systems V,eds. Jacoby G.H. & Barnes J. (San Francisco: ASP), 17 (`XSPEC`)
Arnaud K.A., 2001, ApJ, submitted
Arnaud M. & Evrard A., 1999, MNRAS, 305, 631
Beers T.C., Flynn K., Gebhardt K., 1990, AJ 100, 32 (`ROSTAT`)
Bertin E., Arnouts S., 1996, A&AS, 117, 393 (`SExtractor`)
Böhringer H., Schueker P., Guzzo L., et al., 2001, A&A, 369, 826
D'Agostino R. B. & Stephens M. A., 1986, Goodness-of-fit Techniques (New York: Marcel Dekker)
Danese L., De Zotti G., di Tullio G., 1980, A&A, 82, 322
Dickey J.M. & Lockman F.J., 1990, ARA&A, 28, 215
Dos Santos S. et al, 2003
Dressler A., Oemler A., Couch W., et al., 1997, ApJ, 490, 577
Efron, B., Tibshirani, R., 1986, Stat. Sci., 1, 54
Fairley B.W., Jones L.R., Scharf C., et al. 2000, MNRAS, 315, 669
Gladders M.D., Yee H.K.C., 2000, AJ, 120, 2148
Gonzalez A.H., Zaritsky D., Dalcanton J.J., & Nelson, A. E., 2001, ApJS, 137, 117
Gunn J.E., Hoessel J.G., & Oke, J. B., 1986, ApJ, 306, 30
Jean C., et al. 2003, in preparation
Kinney A., Calzetti D., Bohlin R., et al., 1996, ApJ, 467, 38
Kurtz M.J. & Mink D.J., 1998, PASP, 110, 934
Le Fèvre O., Mellier Y., McCracken H.J., et al., 2001, in "New Era of Wide-Field Astronomy", Eds. R.G. Clowes, A.J. Adamson, G.E. Bromage, ASP conference series, Vol. 232, p449
McCracken H.J., Radovich M., Bertin E., et al., 2003, A&A, submitted
Pierre M., Valtchanov I., Dos Santos S., et al. 2003, (paper I)
Pisani A., 1993, MNRAS, 265, 706
Postman M., Lubin L. M., Gunn J. E., et al., 1996, AJ, 111, 615
Postman M., Lubin L., Oke J., 1998, AJ, 116, 560
Raymond J.C., Smith B.W., 1977, ApJS 35, 419
Refregier A., Valtchanov I., Pierre M., 2002, A&A, 390, 1
Reiprich T.H. & Böhringer H., 2002, ApJ, 567, 716
Rosati P., Borgani S., Norman C., 2002, ARAA, 40, 539
Scharf C., 2002, ApJ, 572, 157
Silverman B., 1986, Density Estimation for Data Analysis and Statistics (London: Chapman & Hall)
Stanford S.A., Elston R., Eisenhardt P.R., et al., 1997, AJ, 114, 2232
Starck J.-L. & Pierre M., 1998, A&AS 128, 397
Starck J.-L., Murtagh F., Bijaoui A., 1998, Image Processing and Data Analysis. The Multiscale Approach. Cambridge University Press
Tonry J.L., Davis M., 1979, AJ, 43, 393
Valtchanov I., Pierre M., Gastaud R., 2001, A&A, 370, 689
Willis J. et al., 2003, in preparation
Wu X.-P., Xue Y.-J., Fang L.-Z., 1999, ApJ, 524, 22
Xue Y.-J. & Wu X.-P., 2000, ApJ, 538, 65